Atmos. Meas. Tech. Discuss., 8, 4347–4377, 2015
www.atmos-meas-tech-discuss.net/8/4347/2015/
doi:10.5194/amtd-8-4347-2015


Atmospheric Measurement Techniques Discussions



# Characterization of downwelling radiance measured from the ground-based microwave radiometer using the theoretical reference data

**M.-H. Ahn[1], H. Y. Won[1], D. Han[1], Y.-H. Kim[2], and J.-C. Ha[2]**

[1]Department of Atmospheric Science and Engineering, Ewha Womans University, Ewha-Yeodae-Gil 52, Seodaemoon-Gu, Seoul, Republic of Korea
[2]Forecast Research Laboratory, National Institute of Meteorological Research/Korea Meteorological Administration, 33, Seohobuk-ro, Seogwipo Jeju-do, Republic of Korea

Received: 11 February 2015 – Accepted: 13 April 2015 – Published: 29 April 2015

Correspondence to: M.-H. Ahn (terryahn65@ewha.ac.kr)

Published by Copernicus Publications on behalf of the European Geosciences Union.







## Abstract

The ground-based microwave sounding radiometers installed at 9 weather stations of Korea Meteorological Administration alongside with the wind profilers have been operated for more than 4 years. Here we introduce a process to assess the characteristics of the instrument calibration by comparing the measured brightness temperature (Tb) with the theoretical reference data, which are prepared by the radiative transfer simulation with the temperature and humidity profiles from the numerical weather prediction model. Based on the three years of data, from 2010 to 2012, we were able to characterize the effects of the absolute calibration, the thick clouds, and the frequency calibration to the quality of the measured Tb. When the three effects are properly considered, including the frequency adjustment which is estimated using the simulated Tb, the measured and simulated Tb show an excellent agreement. The regression coefficients are better than 0.97 along with the bias value of better than 0.5 K. However, the variability given as the SD of difference between the measured and simulated Tb, show a relatively large value at the lower observation frequencies, as large as 2.6 K at the 51.28 GHz channel, while they improve with the increasing frequency.

## 1 Introduction

The potential benefits of ground-based remote sensing instruments such as ceilometer, cloud radar, wind profiler, and passive radiometers are quite well understood and have attracted attention to the continuous efforts for an improvement (Wilczak et al., 1996; WMO, 2006; Cimini et al., 2015). Among those instruments, the ground-based microwave sounding radiometer (hereafter the radiometer) which takes measurement of the downwelling radiances (in the form of brightness temperature, Tb) in the microwave region has been used to obtain the vertical information of temperature ($T$) and humidity ($q$) (Cimini et al., 2003; Löhnert and Maier, 2012; Cadeddu et al., 2013). Its cost efficiency, the capability of autonomous operation, and high temporal resolution





AMTD
8, 4347–4377, 2015



with the relatively high accuracy are the most important advantages that have attracted a variety of users. For example, Knupp et al. (2009) show that the high temporal resolution data from the radiometer could resolve the rapidly changing thermodynamic structure of transitioning boundaries, including cold fronts, gust fronts, bores, and gravity waves. It is a significant potential benefit of the radiometer over radiosondes to be able to detect the thermodynamic changes occurring on very short time scales, on the order of 1–10 min, which are far too short to be captured by radiosondes.

On the other hand, the radiometer is also characterized by the its limited information contents which are mainly located in the lower atmosphere and by the less optimal vertical resolution (Löhnert et al., 2009; Candlish et al., 2012; Cadeddu et al., 2013). Due to the limitation of information contents within the lower atmosphere, the retrieval accuracy of the radiometer usually decreases with increasing altitude (Cadeddu et al., 2002; Hewison, 2006; Löhnert and Maier, 2012). Also, as the radiometer provides the volumetric measurement while the radiosonde measures the point value with the higher vertical resolution, the radiometer often fails to capture a sharp temperature change, such as the shallow inversion layer (Ware et al., 2003; Löhnert and Maier, 2012). To overcome these limitations, several efforts such as combining with satellite observation (Westwater et al., 1985; Ho et al., 2002), utilizing other ground-based remote sensing instruments (Han and Westater, 1995; Löhnert et al., 2008, 2009), and combination with the numerical weather prediction (NWP) model (Gaussiat et al., 2007) have been applied with a considerable improvements, although not a consolidated approach has been established.

With the expected applications to the nowcasting and utilizations for the NWP model, Korea Meteorological Administration (KMA) has been operating 9 ground-based radiometers since as early as April 2009. The observation sites are selected to complement the radar wind profilers which do not provide the vertical thermodynamic information. Although there have been several attempts to utilize the radiometers in research and operational applications (Ha et al., 2007; Jeon et al., 2008; Won et al., 2009), the application has been limited, partly due to the lack of the instrument characterization





AMTD
8, 4347–4377, 2015



or the least understanding of the derived products. Indeed, since the beginning of the operation a thorough investigation to characterize the instrument calibration or to conduct a rigorous validation of the derived products have not been undertaken. Thus, for a better utilization, characterization of the instrument calibration through the analysis of the measured radiance data is highly desired.

Here, we apply a process to characterize the raw observation data, Tb, for a better understanding of the instrument calibration and to improve our understanding of the characteristics of the radiometer products. To take best advantage of the radiometers, i.e. easy to operate without human intervention, most of the radiometers are operated continuously without interruption except for when the regular absolute calibration should be conducted. On the other hand, as there is no additional reference instrument to be used for the direct comparison, we need to find an indirect approach to characterize the raw data from the instrument. Thus, we utilized the vicarious calibration which compares the measured data with the well characterized reference data. Here, we use the theoretically simulated Tb that are obtained from the radiative transfer calculation with the input $T$ and $q$ profiles which are obtained from the NWP models. Application of the NWP model results for the characterization of the radiometer data has been used before, although it is done for a limited occasions (Liljegren and Lesht, 1996; Cimini et al., 2003; Cadeddu et al., 2013; Güldner, 2013).

The paper is organized as follows. Data used for the characterization along with the methodology including a short description of the radiative transfer model are introduced in Sect. 2. The characteristics of raw data obtained from the comparison between the measured and simulated Tbs are given in Sect. 3 followed by the frequency adjustment necessary to best match between the simulated and measured Tb values are described in Sect. 4. The paper is summarized in Sect. 5 with a few lists of the planned future works.





AMTD
8, 4347–4377, 2015



## 2 Methodology and data

### 2.1 Methodology

One of the straight forward approaches for the characterization of the raw data from an instrument would be the direct comparison with data from the well-characterized reference instrument. As that is not available for the radiometers installed in the KMA weather stations, we use an alternative approach, by comparing the measured radiances with the theoretically simulated ones (Löhnert and Maier, 2012; Güldner, 2013). As the performance of vicarious calibration is highly dependent on the accuracy of the simulated radiances, we need a reliable radiative transfer model (RTM) and the accurate $T$ and $q$ profiles which are used for the input data of RTM. Although well characterized RTM is readily available (see below), it is not usually the case for the high quality $T$ and $q$ profiles, especially for a sufficiently long time period that is required for the correct characterization. Thus, here we use the $T$ and $q$ profiles from the NWP models (hereafter called NWP data) for the calculation of the simulated radiance. To make sure that the NWP data is accurate enough to be used as the reference data, we first compare the NWP data to the $T$ and $q$ profiles obtained by the limited number of radiosonde observations. The simulated Tbs from the RTM simulation with the inputs from the NWP data and from the radionsonde data are also inter-compared to check the effects on the simulated Tb by the difference of the $T$ and $q$ profiles. We, then, assess the calibration characteristics by comparing the measured Tb with the theoretically simulated Tb.

### 2.2 Data

#### 2.2.1 Microwave radiometer

The measured Tb ($Tb^R$) is obtained by a ground-based microwave sounding radiometer manufactured by RPG Radiometer-physics GmbH (hereafter the RPG radiometer)





AMTD
8, 4347–4377, 2015



which has been operated at the Changwon Weather Station (35.17° N and 128.57° E, at 37.15 m above the sea level) of South Korea since 2010. The RPG radiometer has a total of 14 observation frequencies, seven at around the 22.24 GHz water vapor resonance line, and another seven for the 60 GHz oxygen absorption band (RPG, 2013; also refer Table 1).The seven channels around 22.24 GHz are used for the water vapor profiling, while the seven oxygen channels are used for the temperature profiling. Additional products such as the total precipitable water, and the cloud liquid water are also derived by the combination of all fourteen channels (Solheim et al., 1998; Li et al., 1997; Won et al., 2009). The Tb data are obtained every 2–3 s with infrequent interruption for the gain calibration, looking at the internal blackbody installed bottom of the RPG radiometer (RPG, 2013).

The measured Tb is obtained by conversion of the measured downwelling radiance using the calibration curve prepared by through the absolute calibration. For the absolute calibration, four reference signals from the warm and cold targets with the addition of the noise diode signal to each target are used to derive the four unknowns, including gain coefficient, non-linearity factor, background noise, and temperature of the noise diode (RPG, 2013). The warm target is internally installed blackbody and the liquid nitrogen (LN2) is used for the cold target. It is recommended to conduct the absolute calibration whenever the radiometer is newly installed, relocated, or for every 6 months. During the absolute calibration, the most serious source of uncertainty is known to come from frost formed on the surface of reflector which sends the radiation coming from the cold target to the radiometer. Thus, it is recommended to conduct the absolute calibration with a special care during the humid environment. On the other hand, the real time calibration is done by frequent observation of internal blackbody and the noise diode which adds an additional signal to the input radiance to provide a reference radiance value for the absolute calibration (RPG, 2013). During the study period, from 1 January 2010 to 31 December 2012, Tb data are continously available except for a few occasions including a short interruption during the early observation and during the short and regular absolute calibration periods.





AMTD
8, 4347–4377, 2015



### 2.2.2 Vertical profiles of temperature and humidity

As a part of assessment test for the void upper air observation over the southeastern part of Korea to the weather forecasting, an automatic radiosonde equipment has been operated at the Changwon Weather Station since 2012. The radiosonde is Vaisala RS-92 GPS with known accuracy of better than 0.5 K (Nash et al., 2011; Miloshevich et al., 2009). As the radiosonde has been launched for the experimental purpose and thus observational frequency and period are quite variable. For example, during the year 2012, there were two intensive observation periods, one was from 25 June to 29 June and another was from 24 August to 29 August. During these periods, radiosonde was launched 8 times a day, while it was reduced twice a day during the other observation period. Radiosonde data are available since June 2012 and the number of radiosonde data used for the current study is 117. These limited number of available radiosonde data are compared with two different sets of the NWP data, one from hourly KLAPS (Korea Local-area Analysis and Prediction System; NIMR, 2012; Lee et al., 2010) analysis data and another from the six hourly ECMWF (European Center for Medium-range Weather Forecasts) analysis data (Richardson et al., 2013) with the spatial resolution of 0.25° for both the simulated Tbs and vertical temperature profiles. The NWP data are linearly interpolated to the radiometer site using the surrounding four grid points and then vertically interpolated to match the radiometer retrieval altitudes.

A direct comparison in terms of the bias and variability (bias and variability are obtained from the average and SD of the difference between the two values, respectively) between the available radiosonde and the NWP data is summarized in Fig. 1. The biases of the temperature profile between the radiosonde and the NWP data are all within 1 K for at least below about 9 km except near the ground where as large as 1.5 K is found for both NWP data. Overall, the ECMWF data show a warm bias, while the KLAPS data have the cold bias, with the almost the same absolute magnitude. However, if we check the variability as shown in Fig. 1b, the ECMWF data show the smaller value compared to the KLAPS data. Furthermore, the ECMWF data show a quite con-





AMTD
8, 4347–4377, 2015



stant value with the altitude, while the KLAPS data show an increase of the variability with the increasing altitude. Thus, from the direct comparison of the temperature profile, it is concluded that the two NWP data show a satisfactory bias characteristic in relation with the radiosonde uncertainty, while the variability characteristics of the ECMWF data is better than that of the KLAPS data. To assess the effects of these bias and variability characteristics to Tb, the simulated Tb with vertical profiles from both radiosonde and NWP data are also compared (see Sect. 3.1).

### 2.3 Radiative transfer model

For the theoretical calculation of Tb, we use the MonoRTM, a radiative transfer model that has been used for the ARM (Atmospheric Radiation Measurement) program (Clough et al., 2005; Payne et al., 2011). The model can be run to simulate upwelling or downwelling radiance at the given number of monochromatic spectrum for a range of user specified conditions including viewing geometries. Although it can incorporate the default cloud models or user provided cloud parameters for the cloudy condition, simulations for the current study are done with the clear sky assumptions. Utilizing the same physics as LBLRTM, the current version (V5.0) takes advantage of numerous improvements in the computational efficiency, the spectroscopy that utilizes HITRAN 2012, and increased flexibility (refer the home page at http://rtweb.aer.com/monortm_frame.html for details). The accuracy obtained from the comparison with the two frequency radiometer at an ARM sits shows that the SD is known to be better than 0.28 K including both RTM and measurement error (Clough et al., 2005).

## 3 Comparison results

To characterize the raw data, we first assess the comparability of the simulated Tb by using the $T$ and $q$ profiles obtained both from radiosonde and the NWP data at seven frequencies of oxygen absorption band. After the assessment, the measured $Tb^R$ val-





AMTD
8, 4347–4377, 2015



ues are compared with the theoretical Tb values. To better understand the cloud effects on $Tb^R$, comparisons are made for both all sky and clear sky conditions. The cloud affected measurement is detected by an algorithm utilizing downwelling infrared radiance measured at the top of the radiometer with the surface temperature and humidity (Ahn et al., 2015).

### 3.1 Comparison of the simulated Tbs

Similar to the comparisons made for the vertical temperature profiles between the radiosonde and the NWP data, the simulated Tb obtained with those input profiles are compared and summarized in Table 1 and Fig. 2. As expected from the temperature comparisons, Tbs simulated with the ECMWF data ($Tb^E$) show the positive bias while those with the KLAPS data ($Tb^K$) show the negative bias (Table 1). The absolute bias value is relatively larger at the lower frequencies, about 0.8 K, compared to the higher frequencies, about 0.4 K, for both the NWP data. Similarly, the variability decreases with increasing frequency for both NWP data, having better than 1 K at most of the frequencies except at the two lower frequencies having as large as 1.6 K at the 51.25 GHz channel for the ECMWF data.

As expected from the temperature comparison, the variability for $Tb^K$ is larger than that of $Tb^E$ and this is considered a rather significant difference due to the number of data used for the comparison (117 vs. 67). In case of the correlation coefficients, the simulated Tbs show quite a good linear relationship, having better than 0.99 at most frequencies. Along with the bias and variability characteristics, the linearity characteristics between the Tb provide a sufficient background for the further utilization of the simulated Tb with the NWP data. Thus, the calibration and validation of the radiometer could be extended to the cases when radiosonde observations are not available. Here, it corresponds to the radiometer data obtained before June 2012 and to the all other 8 radometers installed at the KMA weather stations.





AMTD
8, 4347–4377, 2015



### 3.2 Measured Tb vs. simulated Tb

Here, we present the results from the comparisons made between $Tb^R$ and the simulated Tbs. Table 2 summarizes the error characteristics in terms of the bias, variability, and correlation coefficients for all frequencies of oxygen absorption band. It is quite an interesting to note that the error characteristics are quite a similar, independent to the input profiles used for the simulated Tb. Overall, the error characteristics are much worse at the lower frequencies. For example, the biases at the two lower frequencies are much larger, close to 10 K, than at the higher frequencies. Accordingly, the regression coefficients are also only about 0.7. Although the comparison gets better at the 53.86 and 54.94 GHz channels, these channels still show a different characteristics compared to those of the higher three frequency channels. Other than the strong dependence of the error characteristics to the frequency channels, there are no significant disparate features with the different simulated Tbs. Thus, based on the variability values shown in Fig. 1 and the error characteristics summarized in Table 2, the simulated Tb with the ECMWF data is mainly used for the further discussions.

For a further error characterization, the scatter plots between $Tb^R$ and $Tb^E$ for the first six frequency channels are analyzed as shown in Fig. 3 (the 58 GHz channel shows an almost identical characteristic with that of the 57.3 GHz channel). From the scatter diagram, several interesting characteristics are identified. First of all, channels at lower frequencies such as 51.26, 52.28, and 53.86 GHz show two distinct data groups, with one group having relatively more data points compared to the other group. The distinction is much clearer at the lowest frequency and diminishes with the increasing frequency, becoming indistinguishable at channels higher than 56.66 GHz. The reason for the separation turns out to be due to an apparent error in the absolute calibration done by using the LN2 during the early period of the instrument operation (see below).

Another interesting feature at these lower channels is that both the two separated groups are away from the one-to-one line that represents a perfect match between the measured and simulated Tb. For example, at the 51.26 GHz channel, one denser





AMTD
8, 4347–4377, 2015



group is closer to the one-to-one line, while another group is much further down from the one-to-one line. On the other hand, at the 53.86 GHz channel, the denser group is much further upward than the other group. It should be mentioned here that the separation and offset from the one-to-one line also occurs at the higher frequencies such as the 54.94 GHz channel, although it is not as clearly visible as the other three lower channels. It turns out that this offset from the one-to-one line is mainly due to the uncertainty in the frequency assignment (Löhnert and Maier, 2012) which will be further described in Sect. 4.

Finally, although the large bias and variability values with lower correlations at the lower frequencies are mainly due to the uncertainties in the absolute calibration and frequency assignment, the variability characteristics require further investigation. As shown in Table 2, at the higher frequency channels, the variability values from the comparison with $Tb^E$ are slightly larger than those obtained by the comparison made with the radiosonde simulation, which could be traced to the variability of the ECMWF data itself. However, at the lower channels, the scatters are much larger with $Tb^E$, showing more points away from the majority of points as shown in Fig. 3. Furthermore, all offset points show the warmer Tb compared to the $Tb^E$ which should be reminded here that this represents the clear sky condition. All these evidences, the warmer Tb and increased scatters with decreasing frequencies, point toward the cloud contamination in $Tb^R$ which will be shown shortly after.

The $Tb^R$ characteristics are more clearly revealed in the time series of the difference between $Tb^E$ and $Tb^R$ as shown in Fig. 4. First of all, there are many data points having large positive differences which are more prominent at the lower frequencies. The deviation is as high as 160 K at the 51.26 GHz channel. The large positive difference is explained by the cloud effects which add more radiation to the background clear sky radiance, resulting in the much higher $Tb^R$ compared to $Tb^E$ representing the clear sky condition (Turner, 2007; Cadeddu and Turner, 2011). The cloud effects decrease with the increasing frequency due to the increased radiation by the oxygen absorption/emission resulting in the increased contribution from the warm lower atmo-





AMTD
8, 4347–4377, 2015



spheric emission to the $Tb^R$. Even with the limited effects, the cloud contaminated data is revealed as the scattered data points in Fig. 3. Thus, for an accurate assessment of the calibration characterization, we need to select data points free from the cloud contamination, even at these oxygen channels. For a further assessment, we select the clear sky data only based on the algorithm using the downwelling infrared radiation measured by the IRT radiometer and surface temperature and humidity (Ahn et al., 2015).

Another interesting feature from the time series shown in Fig. 4 is that the Tb difference during a certain period, such as the period from 10 September 2010 to 31 March 2011, is relatively larger than the other periods. Furthermore, the difference is clearly offset from the difference shown for the other time periods. Based on the instrument maintenance records, the absolute calibrations were indeed done in 10 September 2010 and in 31 March 2011 which are exactly coincident with the points having the large discrepancy. Thus, it is highly suspected that the discontinuity in the error characteristics is mainly due to the uncertainty caused by the mistakes occurred during the absolute calibration done in 10 September 2010. To make sure that the discontinuity is not caused by the uncertainties in the simulated $Tb^E$, the time series of difference between $Tb^R$ and $Tb^K$ (from the KLAPS model) are checked and show the same discontinuity (not shown). Although there is a potential way to rectify erroneous data caused by the faulty absolute calibration, we just treat the data as it is for the further characterizations.

### 3.3 Short summary

The $Tb^R$ characteristics, thus far assessed are summarized in Table 3 which compares the bias and variability obtained with the different datasets prepared after applying different selection criteria. For example, when there are no selection criteria in the comparison data, the bias and variability are the largest, especially at the lower frequencies. However, when the comparison is made with the clear sky data only, there





AMTD
8, 4347–4377, 2015



are significant improvements in the bias, the variability, and correlation coefficient, especially at the lower three frequencies. For example, at the 51.26 GHz channel, the bias and variability improve to 0.9 and 6.8 K, respectively, while the regression coefficient is better than 0.86. The similar characteristics are also evident at the 52.28 GHz channel. However, at the 53.86 GHz channel, although the variability and correlation coefficient are improved significantly, the bias improvement is not that impressive. It is also true for the channels near the center of the oxygen band which are not very sensitive to the presence of the clouds.

When the data are further screened for the faulty calibration period, there are significant improvements in the comparison results, again at the lower three frequencies. As shown in Fig. 5, which shows the scatter plot between $Tb^E$ and $Tb^R$ for the four lower frequency channels with the dataset without the cloudy and the faulty calibration period, the correlation coefficient shows a dramatic improvement at the 51.26 GHz channel, from 0.86 to 0.97 along with a significant improvement of the variability (from 6.8 and 2.6 K). At the higher frequencies, the improvement is not that dramatic, although it is still significant (all five higher frequency channels show less than 1 K). On the other hand, the biases at the four lower frequencies degrade slightly, even with those dramatic improvements of the variability and correlation coefficient. This is due to the false compensation of the bias characteristics by the faulty calibration data. For example, as shown in Fig. 5, it is easily recognized that one of the two distinct data groups shown in Fig. 3 is due to the faulty calibration and is successfully removed in Fig. 5. However, with the removal of the faulty data, it is clear that the remaining data points are further away from the one-to-one line, resulting in the bias increase. Thus, it should be emphasized here that the true bias characteristics are only revealed by the comparison data which are free from cloud contamination and from the faulty absolute calibration. In the next section, it will be shown that this relatively large bias in the oxygen wing bands is mainly due to the uncertainties in the frequency calibration.





AMTD
8, 4347–4377, 2015



## 4 Frequency adjustment

As shown in Fig. 5, even after removal of data contaminated by the faulty calibration and cloud contamination, $Tb^R$ and $Tb^E$ show a clear offset from the one-to-one line with the relatively small variability. The apparent systematic bias is also shown in the similar microwave radiometers (Hewison et al., 2006; Löhnert and Maier, 2012), with the most plausible causes are traced to the uncertainty in the frequency calibration. Although there are retrieval algorithms that rely on an empirical method which are not significantly affected by the frequency uncertainty, accurate frequency information is important background information for the retrieval of geophysical parameters and for the application into the data assimilation. Thus, it is highly important to characterize the magnitude and characteristics of the apparent frequency shift for each affected frequency channels.

To assess the necessary frequency shift, we search a new frequency value which gives the least difference between the measured Tb and simulated Tb. And then the comparison between the new frequency value and vendor-provided frequency value provides the characteristics of the frequency shift. For each frequency band, we first select the clear sky $Tb^R$ with free of the faulty absolute calibration in order to minimize uncertainties other than the frequency uncertainty. Then the NWP data corresponding to the observation time of the clear sky $Tb^R$ are used to simulate a hyperspectral theoretical Tb values as a function of frequency values. Once the theoretical Tb spectrum is prepared, the measured $Tb^R$ is used to find the best matching frequency value which gives the least difference between the measured Tb and simulated Tb. As the theoretical Tb spectrum covers all four frequency channels, the best matching frequency for each channel is simultaneously found. The difference between the vendor-provide frequency value and newly found frequency value is considered as the uncertainty in the frequency calibration. To increase the characterization accuracy, we use all of the selected data and also utilize both the ECMWF and KLAPS data to check the NWP





AMTD
8, 4347–4377, 2015



model dependence of the frequency deviation. The results from all selected individual cases are used to derive the bias and variability and are summarized in Table 4.

One of the important findings, as demonstrated in Table 4, is that there is a clear indication of frequency deviation for all four frequency bands. For example, the adjusted frequencies with the $Tb^E$ data are deviated from the vendor-provided frequencies, as much as 0.15 GHz at the 51.26 GHz channel and as small as 0.06 GHz at the 54.94 GHz channel. The deviations at the four given frequency channels are all within the bandwidth (0.4 GHz) of the each frequency channel. However, as the variability of the deviation, given as its SD value, is smaller than the deviation, it could be safely stated that the deviation is a real. The indication is further supported by the results obtained from the KLAPS data, which also give a significant deviation of the frequency value with the smaller variability. For example, at 51.26 GHz, the estimated deviation is 0.09 GHz with its SD of 0.07 GHz. If we compare the averaged deviation estimated by the two simulated Tb values and their SD, the averaged deviations are all comparable and indicate a clear deviation from the vendor-provided frequency values.

Although the frequency adjustment is seemingly small, in view of its broad bandwidth, there is a significant improvement in the Tb comparison between the simulated and measured values as shown in Table 5. For the given four frequency bands, $Tb^E$ corresponding to the adjusted frequency and $Tb^R$ is in much better agreement, as shown by the significant reduction of bias. For the cases with the ECMWF data, bias at all four frequency bands become almost 0.0 (they are 0.2, 0.00, −0.00, and −0.00 K, compared to the values of 4.6, 3.7, 6.4 and 1.7 K when the original frequency values are used). Similar significant improvements with the KLAPS data are also clearly demonstrated. The improvement is primarily due to the strong sensitivity of Tb to the frequency change, a small change in frequency value introduces a significant change in Tb, in this frequency range. On the other hand, the variability remains almost the same, as expected, even after the frequency adjustment. This clearly demonstrates that the frequency adjustment is related to the systematic uncertainty and indeed does not affect the random component. Thus, a careful frequency calibration in this region





AMTD
8, 4347–4377, 2015



is an important prerequisite for the accurate calibration of the measured radiances. Here, however, it should be mentioned that an improved version of the RPG radiometer is known to solve the frequency uncertainty issue all together with a new calibration approach (T. Rose, personal communication, 2014).

## 5 Summary

Nine ground-based microwave sounding radiometers of KMA have been operated since 2010 without a rigorous sensor characterization. For a better utilization of the measurement data, a vicarious calibration process to assess the calibration accuracy of the radiometers has been applied. The reference measurements for the vicarious calibration, the theoretical downwelling radiances (or Tbs), are prepared by the radiative transfer modelling with the input temperature and humidity profiles from the NWP data. Before its application, the simulated Tb with the NWP data is validated with the simulated Tb with the radiosonde observation data. For current study, three years of measurement data from the RPG radiometer being operated at the Changwon Weather Station since 2010 along with the limited number of radiosonde observations and continuous NWP data (from KLAPS and ECMWF) are utilized.

Direct comparison between the theoretical Tb and measured Tb revealed the three important characteristics associated with the instrument calibration. First of all, when the absolute calibration is not properly performed, the intercomparison between the measured and simulated Tbs reveals a clear offset in the measured Tb. Another important finding is that the channels at the edges of the oxygen band have a systematic bias that is traced to the frequency shifts as the main cause. Although the absolute values of the frequency shifts are seemingly small, the shifts introduce a rather large discrepancy between the measured and simulated Tbs. It is further showed that the shifts could be corrected by the high resolution theoretical radiances with the significantly reduced Tb discrepancies. Finally, the clouds with an appreciable optical thickness could introduce a significant uncertainty in the comparison results which require a solid cloud





AMTD
8, 4347–4377, 2015



detection algorithm for a better characterization of the instrument calibration. With the removal of the three important degrading components, the comparison results between the measured and simulated Tbs agree with the better than 1 K in the bias and variability, except at the two lowest frequencies which have the variability value of about 2.6 K which requires a further investigation.

With the same application process, we plan to expand the assessment activities to the other radiometers being operated at other weather stations. Through the activities, overall quality of the measurement data along with the identification of necessary improvements for a better utilization of the instruments could be derived. Also, with the microwave sounding radiometer that is manufactured by different company and had been operated at the same weather station for a limited period of time, we would be in better position to understand the issues related with frequency shift, such as effects on the temperature retrieval. Finally, a similar approach, but with an additional care for the cloudy data, could be used for the water vapor channels. However, it should be mentioned here that even the characteristics of instrument calibration could be analyzed with the NWP data, it would be always better to have a sufficient number of in situ observation data such as the radiosonde observation. This would be more important for the evaluation of the retrieval performance.

*Acknowledgements.* The current work is supported by the "Development and application of technology for weather forecast (NIMR-2013-B-1)" of the National Institute of Meteorological Research (NIMR).

## References

Ahn, M.-H., Han, D., Won, H. Y., and Morris, V.: A cloud detection algorithm using the downwelling infrared radiance measured by an infrared pyrometer of the ground-based microwave radiometer, Atmos. Meas. Tech., 8, 553–566, doi:10.5194/amt-8-553-2015, 2015.

Candlish, L. M., Raddatz, R. L., Asplin, M. G., and Barber, D. G.: Atmospheric temperature and absolute humidity profiles over the Beaufort Sea and Amundsen Gulf from a microwave radiometer, J. Atmos. Ocean. Tech., 29, 1182–1201, 2012.





AMTD
8, 4347–4377, 2015



Cadeddu, M. P. and Turner, D. D.: Evaluation of water permittivity models from ground-based observations of cold clouds at frequencies between 23 and 170 GHz, IEEE T. Geosci. Remote, 49, 2999–3008, 2011.

Cadeddu, M. P., Peckham, G. E., and Gaffard, C.: The vertical resolution of ground-based microwave radiometers analyzed through a multiresolution wavelet technique, IEEE T. Geosci. Remote, 40, 531–540, 2002.

Cadeddu, M. P., Liljegren, J. C., and Turner, D. D.: The Atmospheric radiation measurement (ARM) program network of microwave radiometers: instrumentation, data, and retrievals, Atmos. Meas. Tech., 6, 2359–2372, doi:10.5194/amt-6-2359-2013, 2013.

Cimini, D., Westwater, E., Han, Y., and Keihm, Y.: Accuracy of ground-based microwave radiometer and balloon-borne measurements during the WVIOP2000 field experiment, IEEE T. Geosci. Remote, 41, 2605–2615, 2003.

Cimini, D., Nelson, M., Güldner, J., and Ware, R.: Forecast indices from a ground-based microwave radiometer for operational meteorology, Atmos. Meas. Tech., 8, 315–333, doi:10.5194/amt-8-315-2015, 2015.

Clough, S. A., Shephard, M. W., Mlawer, E. J., Delamere, J. S., Iacono, M. J., Cady-Pereira, K., Boukabar, S., and Brown, P. D.: Atmospheric radiative transfer modeling: a summary of the AER codes, J. Quant. Spectrosc. Ra., 91, 233–244, doi:10.1016/j.jqsrt.2004.05.058, 2005.

Gaussiat, N., Hogan, R. J., and Illingworth, A. J.: Accurate liquid water path retrieval from low-cost microwave radiometers using additional information from a lidar ceilometer and operational forecast models, J. Atmos. Ocean. Tech., 24, 1562–1575, 2007.

Güldner, J.: A model-based approach to adjust microwave observations for operational applications: results of a campaign at Munich Airport in winter 2011/2012, Atmos. Meas. Tech., 6, 2879–2891, doi:10.5194/amt-6-2879-2013, 2013.

Ha, J.-C., Lee, J.-S., Lee, Y. H., Lee, H.-C., and Chang, D.-E.: Production of the high-resolution reanalysis data using KLAPS, Proceedings of the Spring Meeting of KMS, 29–30 April 2010, Geryong, Korea, 227–228, 2010 (In Korean with English abstract).

Han, Y. and Westwater, E.: Remote sensing of tropospheric water vapor and cloud liquid water by integrated ground-based sensors, J. Atmos. Ocean. Tech., 12, 1050–1059, 1995.

Hewison, T.,: 1D-VAR retrieval of temperature and humidity profiles from a ground-based microwave radiometer, IEEE T. Geosci. Remote, 45, 2163–2168, 2007.





AMTD
8, 4347–4377, 2015



Ho, S.-P., Smith, W., and Huang, H.-L.: Retrieval of atmospheric-temperature and water-vapor profiles by use of combined satellite and ground-based infrared spectral-radiance measurements, Appl. Optics, 41, 4057–4069, 2002.

Jeon, E.-H., Kim, Y.-H., Kim, K.-H., and Lee, H.-S.,: Operation and application guidance for the ground-based dual-band radiometer, Atmosphere, 18, 441–458, 2008 (in Korean with English abstract).

Knupp, K. R., Coleman, T., Phillips, D., Ware, R., Cimini, D., Vandenberghe, F., Vivekanandan, J., and Westwater, E.: Ground-based passive microwave profiling during dynamic weather conditions, J. Atmos. Ocean. Tech., 26, 1057–1073, 2009.

Lee, Y. H., Ha, J.-C., Lee, J.-S., Lee, H. C., and Chang, D.-E.: The Korean Local Reanalysis: Preliminary Result (2008–2009), The 3rd THORPEX-Asia Science Workshop and ARC-7 meeting, 3–5 June 2010, Jeju, Korea, 2010.

Li, L., Vivekanandan, J., Chan, C., and Tsang, L.: Microwave radiometric technique to retrieve vapor, liquid and ice, Part I – Development of a neural network-based inversion method, IEEE T. Geosci. Remote, 35, 224–236, 1997.

Liljegren, J. C. and Lesht, B. M.: Measurements of integrated water vapor and cloud liquid water from microwave radiometers at the DOE ARM Cloud and Radiation Testbed in the US southern Great Plains, Proc. Int. Geophys. Rem. Sens. Symp., 96, 1675–1677, 1996.

Löhnert, U. and Maier, O.: Operational profiling of temperature using ground-based microwave radiometry at Payerne: prospects and challenges, Atmos. Meas. Tech., 5, 1121–1134, doi:10.5194/amt-5-1121-2012, 2012.

Löhnert, U., Crewell, S., Krasnov, O., O'Connor, E., and Russchenberg, H.: Advances in continuously profiling the thermodynamic state of the boundary layer: integration of measurements and methods, J. Atmos. Ocean. Tech., 25, 1251–1266, 2008.

Löhnert, U., Turner, D. D., and Crewell, S.: Ground-based temperature and humidity profiling using spectral infrared and microwave observations. Part I: Simulated retrieval performance in clear-sky conditions, J. Appl. Meteorol. Climatol., 48, 1017–1032, 2009.

Miloshevich, L. M., Vömel, H., Whiteman, D. N., and Leblanc, T.: Accuracy assessment and correction of Vaisala RS92 radiosondes water vapor measurements, J. Geophys. Res., 114, D11305, doi:10.1029/2008JD011565, 2009.

Nash, J., Oakley, T., Vömel, H., and Wei, L.: WMO intercomparison of high quality radiosonde systems, Yangjiang, China, 12 July–3 August 2010, WMO/TD-No. 1580, WMO, 248 pp., 2011.





AMTD
8, 4347–4377, 2015



NIMR: Development and application of technology for weather forecast(IV), National Institute of Meteorological Research, Seoul, Republic of Korea, Report-11-1360395-000350-09, 2012 (in Korean).

Payne, V. H., Mlawer, E. J., Cady-Pereira, K. E., and Moncet, J.-L.: water vapor continuum absorption in the microwave, IEEE T. Geosci. Remote, 49, 2194–2208, doi:10.1109/TGRS.2010.2091416, 2011.

Richardson, D. S., Bidlot, J., Ferranti, L., Haiden, T., Hewson, T., Janousek, M., Prates, F., and Vitart, F.: Evaluation of ECMWF forecasts, including 2012–2013 upgrades, technical memorandum No. 710, ECMWF, Reading, Berkshire, UK, 55 pp., 2013.

RPG: Instrument Operation and Software Guide – Principle of Operation and Software Description for RPG standard single-polarization radiometers, RPG, 128 pp., available at http://www.radiometer-physics.de/rpg/html/docs/RPG_MWR_STD_Software_Manual.pdf, last access: 27 April 2015.

Solheim, F., Godwin, J. R., Westwater, E. R., Han, Y., Keihm, S. J., Marsh, K., and Ware, R.: Radiometric profiling of temperature, water vapor and cloud liquid water using various inversion methods, Radio Sci., 33, 393–404, 1998.

Turner, D. D.: Improved ground-based liquid water path retrievals using a combined infrared and microwave approach, J. Geophys. Res., 112, D15204, doi:10.1029/2007JD008530, 2007.

Ware, R., Carpenter, R., Güldner, J., Liljegren, J., Nehrkorn, T., Solheim, F., and Vandenberghe, F.: A multichannel radiometric profiler of temperature, humidity, and cloud liquid, Radio Sci., 38, 8079, doi:10.1029/2002RS002856, 2003.

Westwater, E., Zhenhui, W., Grody, N., and McMillin, L.: Remote sensing of temperature profiles from a combination of observations from the satellite-based Microwave Sounding Unit and the ground-based profiler, J. Atmos. Ocean. Tech., 2, 97–109, 1985.

Wilczak, J. M., Gossard, E. E., Neff, W. D., and Eberhard, W. L.: Ground-based remote sensing of the atmospheric boundary layer: 25 years of progress, in: Boundary-Layer Meteorology 25th Anniversary Volume, 1970–1995, edited by: Garratt, J. R. and Taylor, P. A., Kluwer Academic Publishers, Dordrecht, the Netherlands, 321–349, 1996.

WMO: Operational aspects of different ground-based remote sensing observing techniques for vertical profiling of temperature, wind, humidity and cloud structure: a review, WMO/TD-No. 1309, 37 pp., 2006.





AMTD
8, 4347–4377, 2015



Won, H. Y., Kim, Y.-H., and Lee, H.-S.: An application of brightness temperature received from a ground-based microwave radiometer to estimation of precipitation occurrences and rainfall intensity, Asia Pac. J. Atmos. Sci., 45, 55–69, 2009.





AMTD
8, 4347–4377, 2015



**Table 1.** Error statistics of the simulated Tb obtained from the radiative transfer simulation with the input profiles of temperature and humidity from the NWP data, compared to the simulated Tb with the input profiles obtained by the radiosonde. (Here and afterwards, the bias and variability are obtained from the average and SD of difference between the two values, respectively).

| Frequency | ECMWF | | | KLAPS | | |
|---|---|---|---|---|---|---|
| (GHz) | Bias | Variability | *R* | Bias | Variability | *R* |
| 51.26 | 0.83 | 1.56 | 0.99 | −0.20 | 1.45 | 0.98 |
| 52.28 | 0.75 | 1.19 | 0.99 | −0.30 | 1.18 | 0.99 |
| 53.86 | 0.43 | 0.34 | 0.99 | −0.40 | 0.79 | 0.99 |
| 54.94 | 0.25 | 0.40 | 0.99 | −0.20 | 0.78 | 0.99 |
| 56.66 | 0.30 | 0.62 | 0.99 | −0.00 | −0.90 | 0.99 |
| 57.30 | 0.33 | 0.68 | 0.99 | −0.00 | 0.94 | 0.99 |
| 58.00 | 0.37 | 0.72 | 0.99 | −0.01 | 0.97 | 0.99 |





AMTD
8, 4347–4377, 2015



**Table 2.** Error statistics of the radiometer Tb compared to the simulated Tb using the limited number of radiosonde data (117 data points) and ECMWF and KLAPS data (4384 and 37 230, respectively).

| Frequency | Radiosonde | | | ECMWF | | | KLAPS | | |
|---|---|---|---|---|---|---|---|---|---|
| (GHz) | Bias | Variability | *R* | Bias | Variability | *R* | Bias | Variability | *R* |
| 51.26 | 13.4 | 19.1 | 0.73 | 9.3 | 24.9 | 0.65 | 8.4 | 13.1 | 0.74 |
| 52.28 | 10.6 | 14.8 | 0.75 | 7.3 | 19.3 | 0.68 | 6.6 | 10.2 | 0.77 |
| 53.86 | 7.7 | 3.4 | 0.94 | 7.0 | 4.9 | 0.92 | 6.8 | 2.4 | 0.97 |
| 54.94 | 1.5 | 0.7 | 0.99 | 1.6 | 1.2 | 0.99 | 1.7 | 0.7 | 0.99 |
| 56.66 | −0.4 | 0.6 | 0.99 | −0.3 | 1.0 | 0.99 | −0.1 | 1.0 | 0.99 |
| 57.30 | −0.5 | 0.6 | 0.99 | −0.3 | 1.0 | 0.99 | −0.2 | 1.1 | 0.99 |
| 58.00 | −0.6 | 0.6 | 0.99 | −0.4 | 1.0 | 0.99 | −0.1 | 1.2 | 0.99 |





AMTD
8, 4347–4377, 2015



**Table 3.** Summary of the comparison results between $Tb^E$ and $Tb^R$ obtained from the dataset without any screening process (Original), after removing cloudy data (Clear sky), and after further screening of data produced during the faulty calibration (Calibration). The number of data points for the three cases are 3972, 2375, and 1767, respectively.

| Frequency | Radiosonde | | | ECMWF | | | KLAPS | | |
|---|---|---|---|---|---|---|---|---|---|
| (GHz) | Bias | Variability | *R* | Bias | Variability | *R* | Bias | Variability | *R* |
| 51.26 | 9.3 | 24.9 | 0.65 | 0.9 | 6.8 | 0.86 | 4.6 | 2.6 | 0.97 |
| 52.28 | 7.3 | 19.3 | 0.68 | 0.8 | 5.4 | 0.90 | 3.7 | 2.1 | 0.98 |
| 53.86 | 7.0 | 4.9 | 0.92 | 5.5 | 1.8 | 0.98 | 6.4 | 0.8 | 0.99 |
| 54.94 | 1.6 | 1.2 | 0.99 | 1.3 | 0.8 | 0.99 | 1.7 | 0.5 | 0.99 |
| 56.66 | −0.3 | 1.0 | 0.99 | −0.3 | 1.0 | 0.99 | −0.1 | 0.8 | 0.99 |
| 57.30 | −0.3 | 1.0 | 0.99 | −0.3 | 1.0 | 0.99 | −0.1 | 0.8 | 0.99 |
| 58.00 | −0.4 | 1.0 | 0.99 | −0.4 | 1.0 | 0.99 | −0.1 | 0.9 | 0.99 |





AMTD
8, 4347–4377, 2015



**Table 4.** The adjusted frequency for the four lowest frequncies by using the ECMWF and KLAPS profiles. The adjusted frequency is obtained by taking averages of the frequencies that gives the best match between the measured Tb and simulated Tb. The numbers within the parentheses is averaged difference and its SD, which are smaller than the average value.

| Frequency | Frequency (GHz) | |
|---|---|---|
| (original) | ECMWF | KLAPS |
| 51.26 | 51.41 (0.15 ± 0.08) | 51.35 (0.09 ± 0.07) |
| 52.28 | 52.34 (0.06 ± 0.04) | 52.33 (0.05 ± 0.03) |
| 53.86 | 53.97 (0.11 ± 0.02) | 53.96 (0.10 ± 0.02) |
| 54.94 | 55.08 (0.14 ± 0.05) | 55.06 (0.12 ± 0.06) |





AMTD
8, 4347–4377, 2015



**Table 5.** The resultant bias and variability of difference between the measured Tb and the simulated Tb corresponding to the new frequencies.

| Frequency | ECMWF | | KLAPS | |
|---|---|---|---|---|
| | Bias | Variability | Bias | Variability |
| 51.41 | 0.02 | 2.64 | 0.02 | 2.66 |
| 52.34 | 0.00 | 2.09 | 0.07 | 2.08 |
| 53.97 | −0.00 | 0.72 | −0.10 | 0.76 |
| 55.08 | −0.00 | 0.50 | −0.00 | 0.64 |





AMTD
8, 4347–4377, 2015



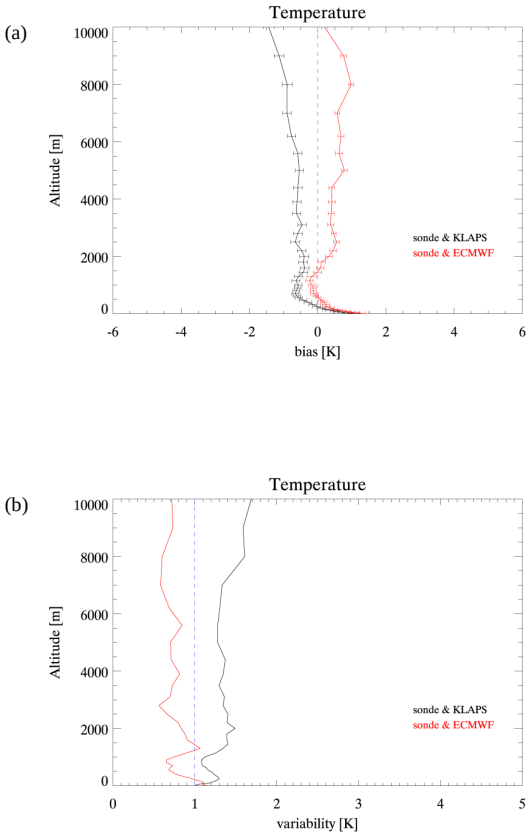


**Figure 1.** The bias **(a)** and the variability **(b)** of the temperature profiles of the NWP data compared to the radiosonde data obtained from June 2012 to July 2013 (total of 117 and 67 data points for KLAPS and ECMWF, respectively). The horizontal error bar in the bias profile represents the SD of mean (red and black solid lines are for the comparison between radiosonde vs. the ECMWF profile and radiosonde vs. the KLAPS reanalysis, respectively).





AMTD
8, 4347–4377, 2015





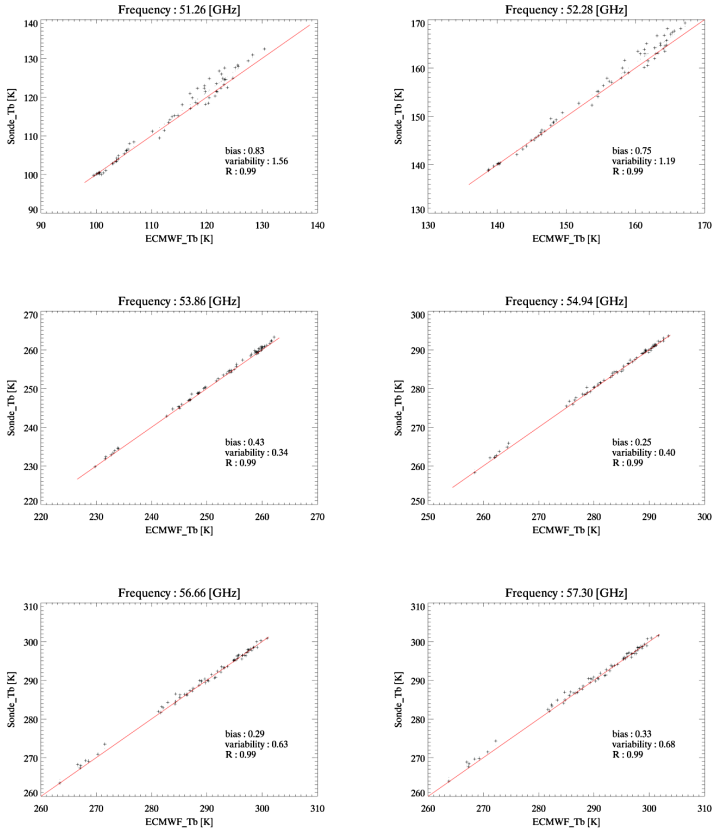


**Figure 2.** Scatter diagram of the simulated Tb using vertical profiles of temperature and humidity from radiosonde vs. ECMWF data for the lower 6 frequency bands.





AMTD
8, 4347–4377, 2015



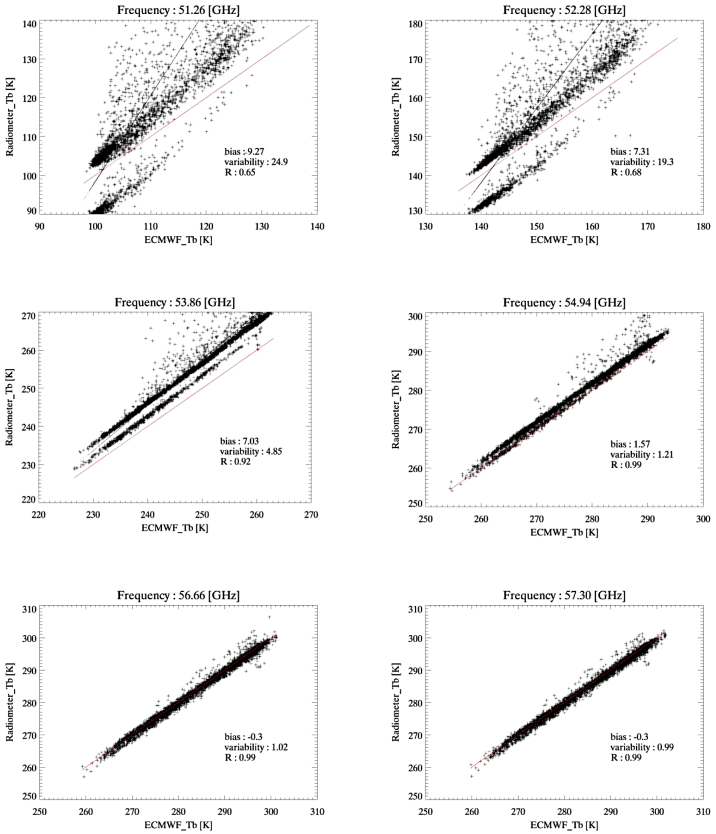


**Figure 3.** Comparison between the radiometer Tb and the simulated Tb with the input profiles of the ECMWF data (red line is the one to one line).





AMTD
8, 4347–4377, 2015





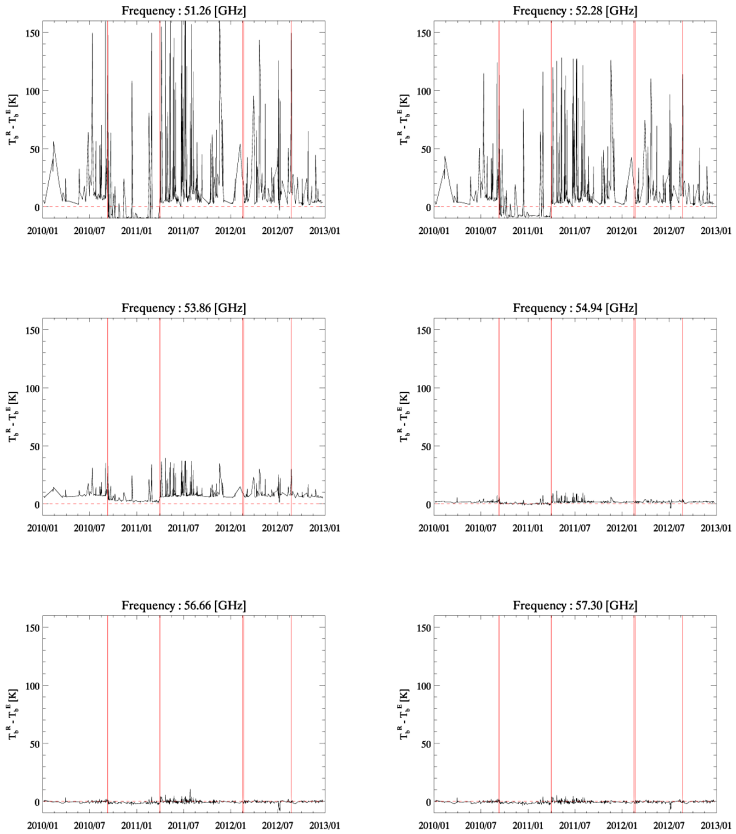


**Figure 4.** Time series of the Tb difference between the RPG radiometer and simulated (with the ECMWF profile) for the six oxygen bands (note the different range of *y* axis). The red vertical bars denote the data when the absolute calibration is performed.





AMTD
8, 4347–4377, 2015



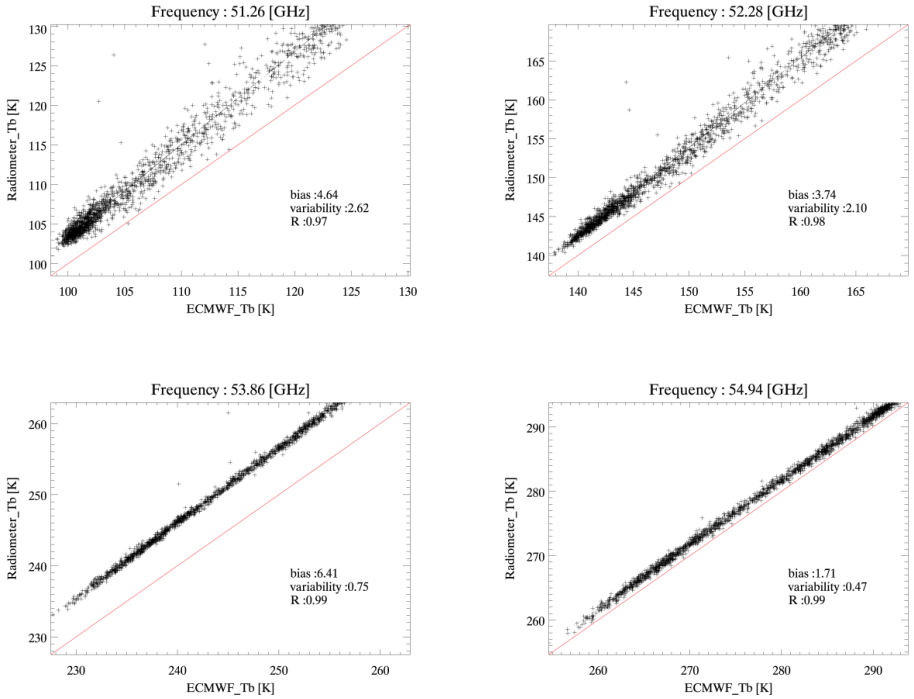


**Figure 5.** Scatter diagram of $Tb^E$ and $Tb^R$ obtained after removing data with the erroneous calibration and contaminated by clouds.





AMTD
8, 4347–4377, 2015